Materials Today Advances 25 (2025) 100566

Contents lists available at ScienceDirect

Materials Today Advances

journal homepage: www.journals.elsevier.com/materials-today-advances/

Making parts on Mars: Laser processing of iron contaminated by regolith simulant

Askar Kvaratskheliya [a,b,c,*], Aleksandr Filimonov [a,b], Bruno Bianchini [b,d], Muchammad Izzuddin Jundullah Hanafi [c,e], Thorsten M. Gesing [c,e], Taisuke T. Sasaki [f], Piter Gargarella [d,g,h], Lutz Mädler [a,b], Ilya Okulov [a,b]

[a] University of Bremen, Faculty of Production Engineering, Badgasteiner Straße 2, 28359, Bremen, Germany
[b] Leibniz Institute for Materials Engineering IWT, Badgasteiner Straße 3, 28359, Bremen, Germany
[c] University of Bremen, MAPEX Center for Materials and Processes, Bibliothekstraße 1, D-28359, Bremen, Germany
[d] Graduate Program in Materials Science and Engineering, Federal University of São Carlos, Rod. Washington Luis, Km 235, 13565-905, São Carlos, SP, Brazil
[e] University of Bremen, Institute of Inorganic Chemistry and Crystallography, Leobener Straße 7, D-28359, Bremen, Germany
[f] Research Center for Magnetic and Spintronic Materials, National Institute for Materials Science, Tsukuba, 305-0047, Japan
[g] Department of Materials Engineering (DEMa), Federal University of São Carlos (UFSCar), Rod. Washington Luis Km 235, 13565-905, São Carlos, SP, Brazil
[h] Center of Characterization and Development of Materials (CCDM), Federal University of São Carlos (UFSCar), Rod. Washington Luis Km 235, 13565-905, São Carlos, SP, Brazil

ARTICLE INFO

Keywords:
Mars
Regolith
Printing
Contamination
Metal matrix composites

ABSTRACT

Manufacturing pure metals on Mars is challenging due to limited energy resources and unavoidable contamination of raw materials and production equipment with the Martian dust (regolith) resulting in impure materials. Understanding the effect of contamination on material properties is crucial for establishing materials manufacturing on Mars. This study investigates the influence of regolith contamination on its processability, and properties of the Fe-based material manufactured via laser powder bed fusion (L-PBF) for potential extraterrestrial applications. To simulate a contamination, water-atomized iron powder was mixed with 1 wt% Martian regolith simulant and processed by L-PBF. It was found the regolith is uniformly distributed within the iron matrix transforming from contaminant to reinforcement material. The crack-free interface between iron and regolith systematically studied using STEM reveals segregation of some elements but absence of notable reaction between matrix and particles. The Fe-regolith composite demonstrate moderate strength and large plastic deformability. The results suggest that unavoidable regolith contamination during production on Mars can be rethink as in-situ resource utilization for manufacturing of regolith reinforced iron matrix composites.

1. Introduction

ISRU (In Situ Resource Utilization) refers to the development of systems that leverage natural resources on extraterrestrial objects [1]. Such an approach allows planning a more advanced mission without the limitations of maximum capacities that can be transferred from Earth to Mars or Moon [2]. The most critical resources for ISRU production are considered to be oxygen, water and propellant [3–6]. But in order to start space industrialization and scale up production structural materials should be manufactured. Many works focus on the production of construction parts by different methods using regolith as a feedstock material for 3D printing, sintering, hot extrusion and other technologies [7–10]. Extraterrestrial soil is considered to be a basis for production of glass, concrete and shielding material for future lunar and martian bases [[11–13]. Another pivotal part of future Mars and Moon missions is the production of metals from regolith; some works already showed its high potential in production iron, aluminium and their alloys using electrochemistry [8,14–16]. One of the most promising metals that can be extracted is considered to be iron, due to the possibility of its refinement with microbes from the extraterrestrial soil [17]. These works demonstrate that it is possible to produce metals in powder form for further use in production routes and is a starting point for space industrialization.

The production of materials with specific mechanical or functional "Enough-to-use" properties by additive manufacturing might be

* Corresponding author.
E-mail address: a.r.kvarts@gmail.com (A. Kvaratskheliya).

https://doi.org/10.1016/j.mtadv.2025.100566
Received 12 September 2024; Received in revised form 13 February 2025; Accepted 21 February 2025
Available online 26 February 2025

necessary in specific cases. Goulas et al. [18] manufactured structural materials from lunar and Martian regolith, delving into the material properties for laser powder bed fusion (L-PBF) and revealing problems associated with the volatility of the porous Martian simulant. Caprio et al. [19] focused on the production of materials from lunar regolith. In the work of Afrouzian et al. [20] a composite made out of Ti6-Al4-V alloy substrate and Martian regolith coating was manufactured, which increased its microhardness. In the work of Liao et al.,[21], a composite material made of AlSi10Mg alloy as a binder and Lunar regolith was additively manufactured. This composite with high concentration of regolith (50 wt%) showed robustness, nonetheless a strong reaction of regolith and matrix led to a decrease in mechanical properties. Al has a strong affinity to oxygen and reduces multiple oxides from the regolith [21]. Therefore, the formation of brittle phases, cracks and pores is observed at the Al-regolith interface what limits the application of Al for metal-regolith composites. The weak interface could even affect the elastic properties of the composites [22,23]. Unlike Al, Fe is less reactive in molten state and does not react intensively with regolith and has the potential to form a strong interface with it. This study systematically addresses the interface issue, along with the inevitable cross-contamination that occurs during manufacturing under Martian conditions.

Cross-contamination is a common problem in additive manufacturing [24]. Due to the dusty environment on Mars [25], cross-contamination of metal with regolith is inevitable. However, contamination of iron with regolith particles the material naturally becomes composite, which can be advantageous. Ferrous matrix composites impregnated with various types of particles demonstrate considerable promise for additive manufacturing. Typically, these composites are infused with carbides, oxides, or fiber-type fillers to enhance their mechanical properties or introduce novel functionalities [26]. A typical material for impregnation can be tungsten, silicon, or titanium carbides, where materials properties were successfully enhanced by introducing such particles [27–29]. Introducing Al_2O_3 in iron matrix is harder, compared to carbides due to the tendency of dissociation of Al_2O_3 particles in the iron during the process [26]. A possible benefit of introducing oxide particles in metal can be altering its structure. L-PBF process for 3D printing 316L austenitic stainless steel/Al_2O_3 nanocomposites resulted in a significant modification of the grain structure and crystallographic texture, leading to the formation of micron/nanoscale equiaxed grains with directional grain growth and improved hardness [30]. Such columnar-to-equiaxed transition effect can be induced by addition of metallic particles [31]. Both extraterrestrial resource utilization and particle-infused ferrous matrices, additive manufacturing continues to advance towards achieving materials with superior performance and versatility.

This study investigates the properties of Fe-regolith metal matrix composite additively manufactured samples L-PBF. Upon metallographic preparation of the as-build samples, the samples undergo comprehensive analysis, including X-ray diffraction (XRD), electron backscattered diffraction (EBSD), scanning electron microscopy (SEM), energy-dispersive X-ray spectroscopy (EDX), transmission electron microscopy (TEM), and μ-computed tomography (μ-CT) scans for microstructural, morphological, and compositional analysis. Microhardness testing and mechanical compression tests evaluate material strength and deformation characteristics.

2. Materials and methods

Iron was chosen as the primary material because of its abundance as metallic component in the regolith, its well-established extraction methods - both electrochemical and biological and its reliability as a resource on Mars [17,32–34]. Accordingly, the initial step involved using high-purity iron powder with a mean particle size of 40 μm (Goodfellow Cambridge Ltd., Huntingdon, England). In the initial step, pure iron powder with a mean particle size of 40 μm (Goodfellow Cambridge Ltd., Huntingdon, England) was utilized. Obtaining pure iron from Martian regolith is unlikely, as refining processes leave permanent contamination due to the complex mix of oxides and minerals inherent in the regolith and complexity of the reduction process [33]. The shape of the metal particles after these processes, as well as grinding, will be irregular, hence iron powder atomized in water was chosen. Examination of the surface of iron particles before mixing with regolith simulant showed that silicon, manganese and chromium oxide nanoparticles were present on the surface. We introduced a contamination by mixing 1 wt% of MGS-1 (Space Resource Technologies, Oviedo, USA) Martian regolith simulant particles ground and sieved to a mean particle size fraction below 12 μm. This contamination level aligns with the complexity of Martian regolith, ensuring that the experimental setup mirrors the impurity levels likely encountered during practical applications, while maintaining controlled and measurable parameters for analysis. Granulometric analysis of the mixture was conducted using SYNC Microtrac (Microtrac Retsch GmbH, Haan, Germany). To ensure a uniform distribution of particles, a Turbula T2F mixing device was employed with a mixing time of 1 h at a frequence of 1 Hz. Subsequently, a preliminary experiment was conducted using $5 \times 5 \times 5$ mm^3 cubes to reveal parameters with low porosity for L-PBF, including laser power, scan speed, hatch spacing, and layer thickness. Laser power ranged from 225 to 325 W with increments of 25 W, while speed varied from 400 to 800 mm/s for powers between 225 and 275 W, from 500 to 900 mm/s for 300 W, and from 600 to 1000 mm/s for 325 W, with a step size of 100 mm/s. To examine the microstructure of the material, surface preparation of the as-built samples was performed. This involved grinding with SiC paper up to 2000 mesh, followed by polishing using a colloidal solution of 0.25 μm Silica Oxide OP-S. The powder after mixing, the closeup of iron particle before mixing and granulometric data of its components are depicted in Fig. 1. For mechanical compression tests, cylindrical compression samples with a diameter of 6 mm and a height of 12 mm were fabricated using following parameters: 300 W and 500 mm/s.

XRD analysis was conducted using a D8 Discover diffractometer (Bruker, Billerica, USA) equipped with $CuK\alpha_{1,2}$ radiation ($\lambda_{K\alpha1}$ = 154.05929 (5) pm, $\lambda_{K\alpha2}$ = 154.4414 (2) pm) in Bragg–Brentano geometry. The measurement was carried out in the range from 15.0 to 120° 2-Theta, with a step size of 0.0149° and an exposure time of 1 s/step using a LynxEye XE-T multi-channel detector. X-ray powder diffraction data were analyzed using the Rietveld method [35]. For this, the fundamental parameters were fitted against a LaB_6 standard material and applied for the Rietveld refinement using the "Diffrac^{Plus} Topas 4 and 6" software (Bruker AXS GmbH, Karlsruhe, Germany). The instrumental reflection broadening was determined using a double-pseudo-Vogt approach with only a Gaussian contribution for the average crystallite size and only a Lorentzian contribution for the micro-strain analysis. A maximum observable average crystallite size (MOACS [36]) of 280 nm was used. During the Rietveld refinements a linear and an air scattering $1/x$ background parameter, the unit-cell parameters, atomic coordinates, and isotropic displacement parameters (B), as well as average crystallite size (ACS) and micro-strain (MS) parameters were optimized for the description of the reflection profile of the phases. The degree of crystallinity (DC) was determined using a single reflection fitting of the broad diffuse scattering contribution and comparing this obtained sum of intensities with those of the nano- and micro-crystalline [37] scattering contribution, assuming the same average scattering power in the Bragg reflections and amorphous scattering contribution [30]. Using the assumption that in a Bragg–Brentano geometry the background measured is in a wide range linear plus air scattering at the lower scattering angles (modeled with a 1/x contribution), then all deviations from that background are caused by the sample. The integrated reflection intensities of the amorphous part are calculated individually and summarized as well as the total intensity of the crystalline (Bragg) reflections are summarized. The DC is, assuming an average scattering factor to be equivalent for both parts, defined as follows:

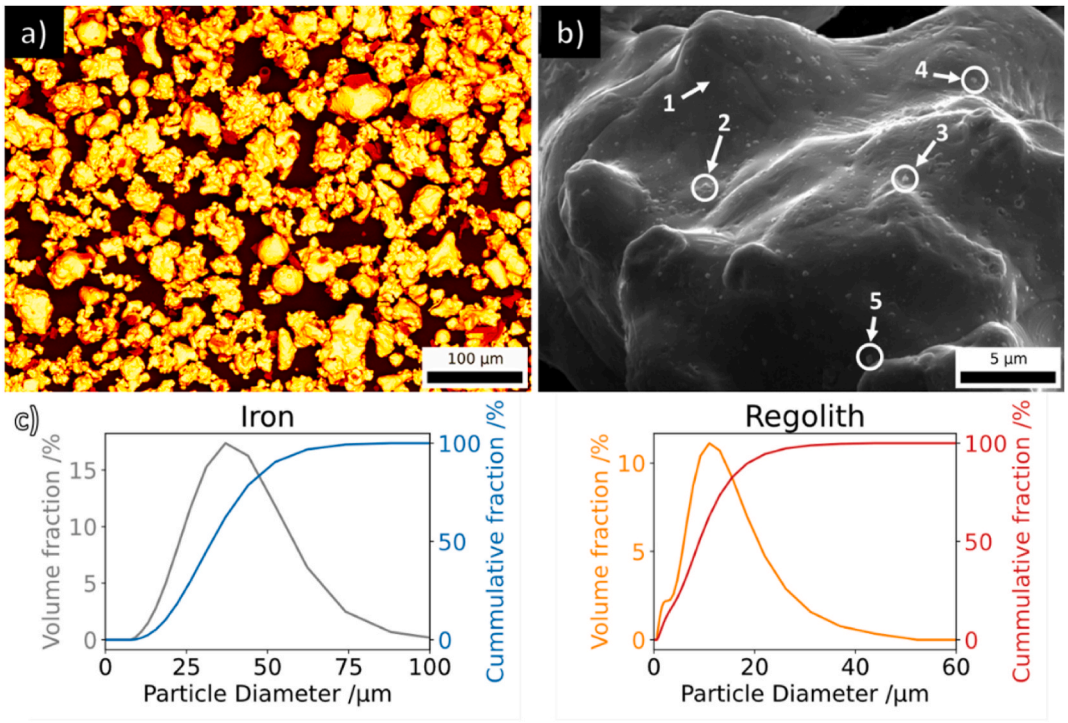

Fig. 1. SEM micrographs of (a) a mixture of Fe and regolith simulant powders with adjusted colours for better visibility of different type of particles (yellow – iron particles, red – regolith simulant particles) used for L-PBF, Detailed view of the particle before mixing with regolith simulant: the area not used for chemical analysis is marked with arrow 1, while nano oxides on the surface are indicated with arrows 2–5 (b), granulometric data of it's components (c). (For interpretation of the references to colour in this figure legend, the reader is referred to the Web version of this article.)

$$DC = \frac{\text{Total intensity of crystalline reflections}}{\text{Total intensity of all reflections}} \text{ x } 100 \text{ wt.\%} \quad (1)$$

The average crystallite size together with the crystallite size distribution has been analyzed by the EnvACS [36] approach using the convoluting method of the smallest and broadest crystallite size distribution by refining the broadening parameter together with the ACS. XRPD Rietveld refinement plot of [36] regolith simulant after grinding and sieving process is shown in Fig. 2.

SEM and EDX using an FEI Quanta 400 microscope integrated with an Oxford Inca Energy 250 EDS system (Thermo Fisher, Waltham, USA) were used to analyze the microstructure and chemical composition of the inclusions before and after compression testing. EBSD measurements were conducted using a Philips REM XL 30 with an Ametek EDAX (Philips, Amsterdam, Netherlands). The analysis included image quality (IQ) and inverse pole figure (IPF) data. The nanometer-scale structural and chemical distribution analysis of the interface was performed using TEM. FEI Nova NanoLab 200 (Thermo Fisher, Waltham, USA) dual-beam SEM and FIB/SEM, FEI Helios G4 UX (Thermo Fisher, Waltham, USA) were used for lamella preparations. Subsequent TEM analysis was conducted with Thermo Fisher Spectra 300 TEM (Thermo Fisher, Waltham, USA), operating at an acceleration voltage of 300 kV and FEI Titan G2 80–200 (Thermo Fisher, Waltham, USA), operating at 200 kV. For in-depth investigation, EDX was employed in scanning-TEM mode (STEM), utilizing a Thermo Fisher Super-X detector. The acquired EDX data underwent thorough analysis using the Thermo Fisher Velox software.

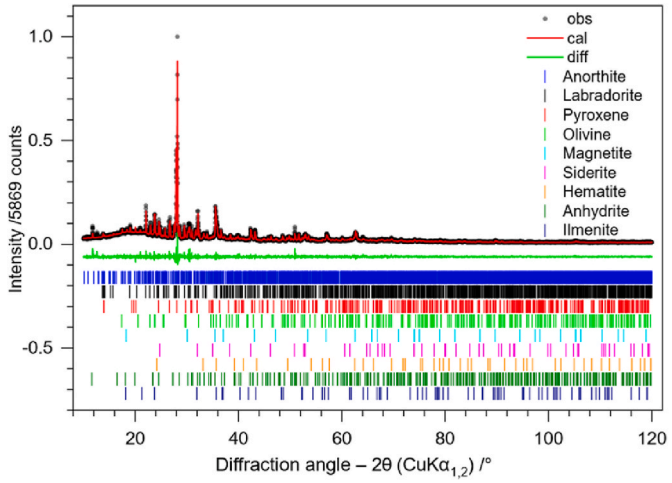

Fig. 2. XRPD plot of the regolith simulant used in this work after undergoing grinding and sieving process.

Further insights into the samples were gained through X-ray µ-CT scans conducted with the ProCon CT-ALPHA system (ProCon X-Ray GmbH, Sarstedt, Germany). The measurement was conducted with a beam energy of 140 kV, an energy flux of 10 W, and a ZEISS HE1 filter. The scanning process involved 360° rotation scans with a step size of 3.89° at a detector resolution of 0.609 µm per pixel. The scan, spanning 17 h, resulted in an image volume of 673 × 886 × 967 voxels. For porosity analysis and image sequence postprocessing, ImageJ software was used [38].

Vickers microhardness testing was performed utilizing a Fischerscope H100C Vickers-hardness tester (Helmut Fischer GmbH, Sindelfingen, Germany) with a load of 9.807 N (HV1). The compression tests of cylindrical samples were conducted using the Instron 5568 (Instron Mechanical Testing Systems, Massachusetts, USA) with load cell of 50 kN. The deformation rate for the test was set at 10^{-3} s^{-1} adhering to the compression DIN EN ISO 6507-1 standard. The tests were performed until the deformation of the sample reached 50 %.

3. Results & discussion

25 cubic samples with varying scanning speed and laser power have

been produced for parameter study. The parameters that allowed to obtain a sample with the lowest porosity were chosen as optimal parameters, which were a scanning speed of 600 mm/s and a laser power of 325 W with porosity close to 0.4 %. Porosity heatmap visualization and baseplate are shown on Fig. 3.

Although the flowability of the powder was enough to form powder bed, the surface of the baseplate had an uneven powder distribution. The presence of these areas subsequently led to uneven surface growth and even greater surface irregularity. The uneven surface areas can be seen in Fig. 3. The heatmap shows that decreasing energy input, achieved by reducing speed and increasing the laser power, results in a more porous material. In this study parameters with minimum porosity were chosen, so heatmap sections with higher power and lower speed were unexamined. SEM images in back-scattered electron (BSE) mode (Fig. 4) showcase the additively manufactured Fe-regolith composite using L-PBF. The SEM analysis revealed dark regolith simulant particles with a spherical form within the iron matrix. An important observation is that all particles exhibit diverse chemical compositions, with the predominant elements being iron (Fe), aluminium (Al), magnesium (Mg), silicon (Si), and calcium (Ca) (Fig. 5). Notably, these particles consist of a mixture of four main minerals: olivine, pyroxene, plagioclase, and basalt glass. This composition aligns with the production method of the Martian regolith simulant used, resulting in a blend of these minerals in approximate proportions [34]. In our investigation, we noted the similarity of the particles in chemical composition, which allowed us to abandon further distinction in this work. The lack of notable chemical interaction between regolith simulant particles and iron matrix at this resolution is evident. The regolith simulant particles exhibit a spherical shape, indicative of melting and solidification processes. Regolith simulant particles larger than 20 μm in diameter display an irregular rounded shape. This can be attributed to agglomeration and remelting of several particles during the L-PBF process. It is important to note that regolith simulant particles mostly show the absence of delamination from the iron matrix. A crack and pore-free interfaces between regolith simulant particles and iron matrix were obtained. Further interface analyses were carried out using SEM-EDX and TEM-EDX. On higher magnification, we can observe nanoparticles, evenly distributed throughout the matrix. These nanoparticles are oxides that have entered the material from the surface of the iron particles. Due to the small particle size, TEM-EDX has been used to provide reliable information about the chemical composition as well as the shape and size of these particles. The nature of these inclusions will be discussed in the later part of the paper.

SEM-EDX analysis of the Fe-regolith composite indicates that the regolith simulant particles are mainly composed of Si, Al, Ca, and O (Fig. 5). Traces of Ca, Al, and Si were undetected in the iron matrix near the iron/regolith interface, indicating the absence of diffusion of these elements into the matrix. The interface between the regolith simulant particles and the iron matrix appears sharp in all elemental contrasts. For a more detailed examination of the interface, TEM-EDX analysis and SAED were performed.

The EBSD analysis data showed that the printed part has a grain structure with elongated grains along the build direction (Fig. 6). The average grain size was calculated using TEAM software for grain analysis and is 16.87 ± 21.05 μm. No pronounced texture was observed. Further structural analysis was conducted with XRD.

X-ray powder data (XRPD) Rietveld refinements were performed for phase quantification of the sample. The refinement results confirm that the ground and sieved MGS-1 regolith simulant used in this work comprises of 9 crystalline phases (Fig. 2). Obtained refinement metrics for analyzed spectra R_{wp}: 11.39, Re_{xp}: 8.02, χ^2: 1.42, DW: 1.20. Phase quantification implies that it predominantly consists of the mineral phases anorthite (38 (2) wt.%) and labradorite (36 (2) wt.%), which belong to the anorthosite group. Pyroxene and olivine contents are found to be significantly lower compared to the original MGS-1 specification sheet. Furthermore, the degree of crystallinity (DC) of the ground and sieved regolith simulant emerged to be 45 (5) wt.%, significantly lower than that of MGS-1 (65 (5) wt.%). XRD analysis of the Fe-regolith composite reveals an absence of detectable regolith simulant in the material, likely due to the detection limits of the device (Fig. 7). XRD Rietveld refinements were also employed on the Fe-regolith sample (99 wt% printed iron with 1 wt% sieved regolith simulant) with next refinement metrics R_{wp}: 11.27, R_{exp}: 8.20 χ^2: 1.37 DW: 1.14. Five pronounced Bragg reflections, along with two minor reflections at 2θ(Cu) of 35.7° and 42.8° are observed in its diffraction pattern. None of these two reflections coincide with any of the strong reflections of the regolith simulant containing phases hinting for any nano- or micro-crystalline contribution.

3.1. Fe-regolith

Fig. 8 shows the acquired TEM SAED of the Fe-regolith composite in the interfacial region. Analysis of the Fe-regolith interface indicates an absence of additional phase formation throughout the sample. The regolith simulant particles predominantly remain in an amorphous state, with partial crystallization highlighted by SAED. The layer thickness is about 20 nm, reflecting a uniform thickness across the particle boundary and confirming that there is no chemical interaction between the particles and the matrix. Different phases within the material are distinguishable in both TEM and EDX.

Fig. 9 (a) shows a low-magnification high-angle annular dark-field STEM image. The iron matrix is imaged with bright contrast in comparison to the regolith simulant, containing the dimly imaged nanoscale particles. The EDS elemental maps obtained from the area surrounded by the dashed line shown in Fig. 9 (b) demonstrate that the nanoscale particles in the regolith simulant are particularly enriched in chromium. It is also noteworthy that the nanoscale particles are discernible with dark imaging contrast even in the iron matrix, which would be expected

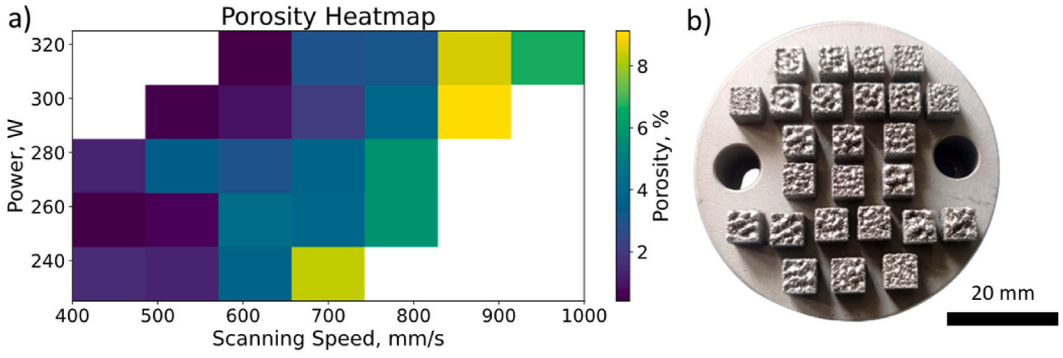

Fig. 3. Porosity heatmap visualization (a) and baseplate with printed cubes which cross sections were used to analyze porosity (b).

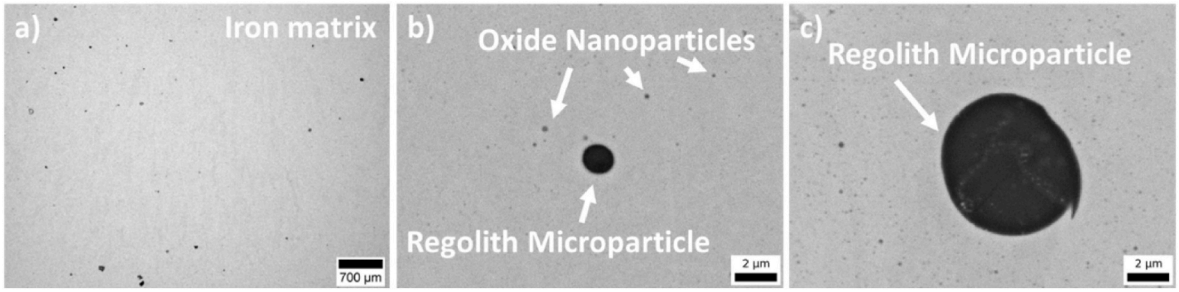

Fig. 4. SEM image of different types of particles in the iron matrix: overview of sample (a), closeup of micro and nanoparticles (b), closeup of a bigger microparticle (c).

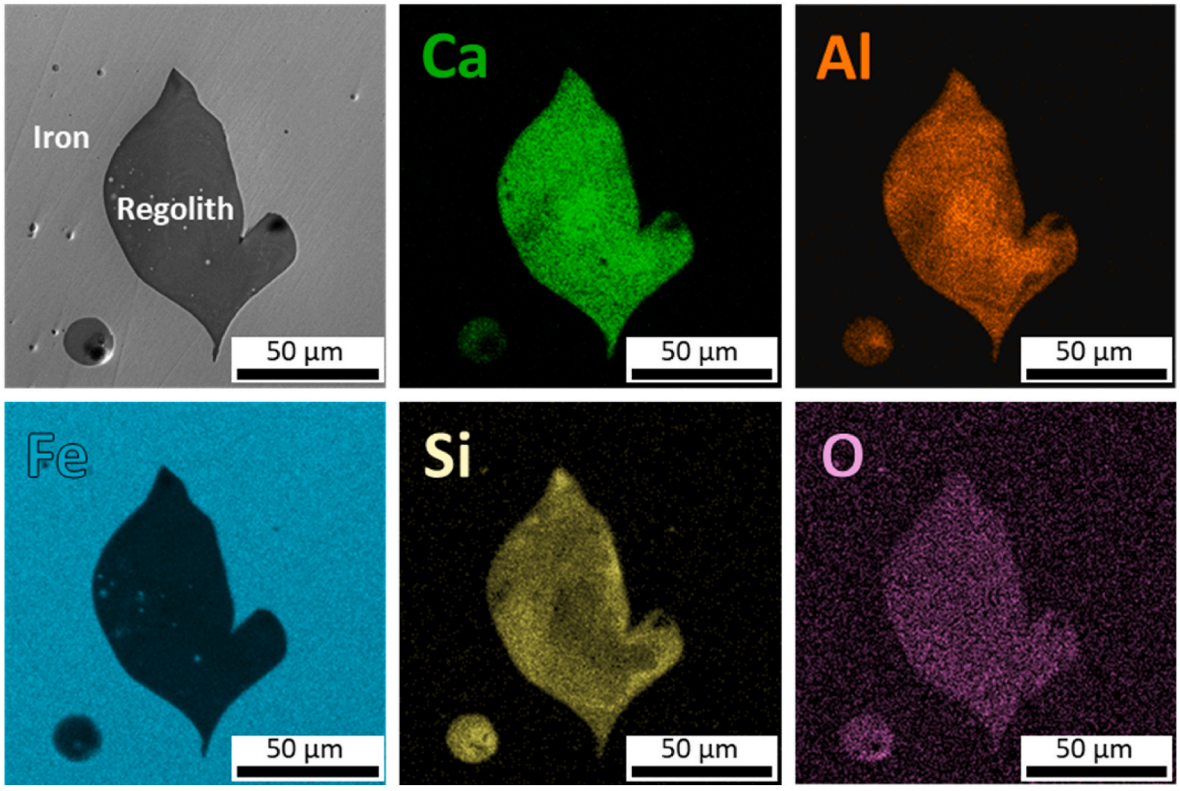

Fig. 5. Elemental mapping of the additively manufactured Fe-regolith composite obtained using SEM-EDX.

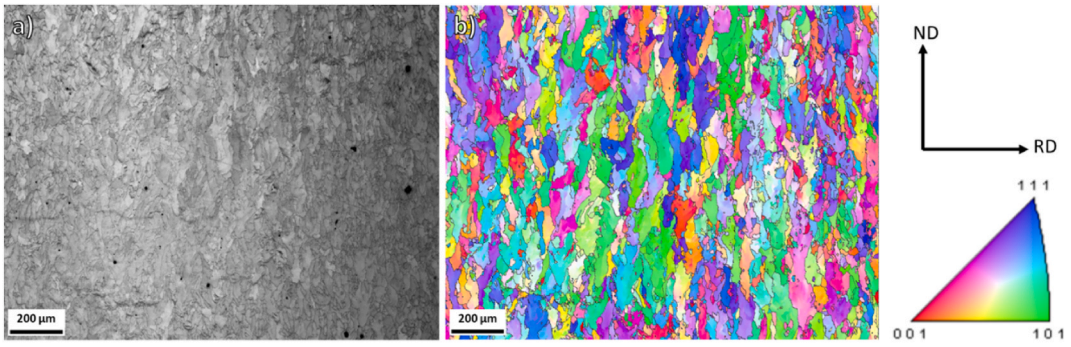

Fig. 6. EBSD images: IQ (a) and IPF (b) of 3D Printed Fe-regolith part.

to be pure iron (Fig. 9 (a)). Spherical particles are Si- and Mn-oxides with an amorphous structure, as evidenced by a microbeam electron diffraction (MBED) pattern obtained from a nanoscale particle indicated by an arrow (Fig. 9 (a)) and EDS elemental maps (Fig. 9 (b)). Since the coarse Mn-oxides are in contact with fine Cr-oxides, it can be postulated that the Cr-oxides have served as heterogeneous nucleation sites for the Mn-oxides. It still remains unclear whether full remelting of particles occurred or not. The melting temperature of Cr-based oxide is rather

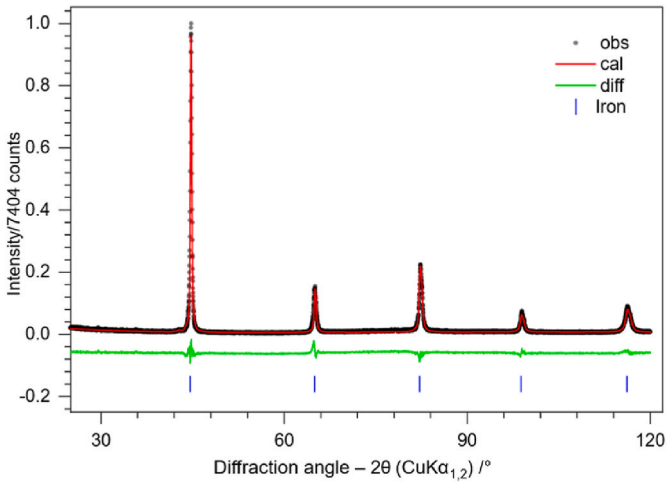

Fig. 7. XRD Rietveld refinement plot of L-PBF Fe-regolith printed part.

high [39]. The EDS elemental maps also show that Cr, Mg, and Al are heterogeneously segregated at the iron/regolith interface. Fig. 9 (c) shows an EDS line compositional profile across an iron/regolith interface denoted as L1 (a). A distinct segregation of Mg, Al, and Cr is evident at the interface, accompanied by a slight enrichment of Si and Ca on the surface of the regolith simulant. The Al concentration at the interface increases from about 11 to 13 at. %, while the Mg concentration spikes from about 3 to 5 at.%. In contrast, in areas with no significant segregation of Mg, Al, and Cr, a slight enrichment of Si and Ca is still evident on the surface of the regolith simulant, as derived from the EDS line compositional profile obtained across the interface denoted as L2 (d).

Fig. 10 shows a reconstructed 3D model of the additively manufactured Fe-regolith composite analyzed sample (a) and its inner pore structure (b) obtained by processing series of binarized images by imageJ software. μ-CT reveals macropores in the material due to lack of fusion and smaller spherical pores associated with gas entrapment, they are depicted as pore type I and pore type II, respectively. The volumetric porosity of the sample was analyzed by binarizing a series of μ-CT images and then using continuous PSD method with imageJ software to calculate pore size distribution (c) [40]. Calculated pore volume fractions indicates ~0.4 vol% porosity and mean pore radius is 4.59 ± 3.62 μm.

Fig. 11 shows the mechanical test results of the additively manufactured Fe-regolith composite probed under compression loading. The 0.2 % offset yield stress of the Fe-regolith composite is 242.4 ± 13.4 MPa. At a strain of 20 %, the Fe-regolith composite exhibits a compressive strength of 486.7 ± 10.6 MPa. The additively manufactured Fe-regolith composite sustained mechanical strain up to 40 %. These mechanical properties compared to pure iron after casting process and worse than L-PBF processed pure iron [41]. The micrograph of the additively manufactured Fe-regolith composite after compression test is shown in Fig. 11. Microhardness HV tests indicate that the material underwent a small hardness increase compared to L-PBF produced iron [42], going from 157 to 169 Vickers Hardness (HV).

During the L-PBF process, both iron particles and regolith simulant undergo melting. However, unlike the behavior observed in the Al-Regolith composite, iron remains chemically inert in relation to regolith simulant particles [21]. This lack of interaction is crucial as it prevents the formation of a brittle phase, which probably decreases the occurrence of cracks or pores at the interface during L-PBF. Previously, Liao et al. [21] highlighted that in aluminum molten pools, remelted regolith simulant tends to aggregate, forming agglomerations with a

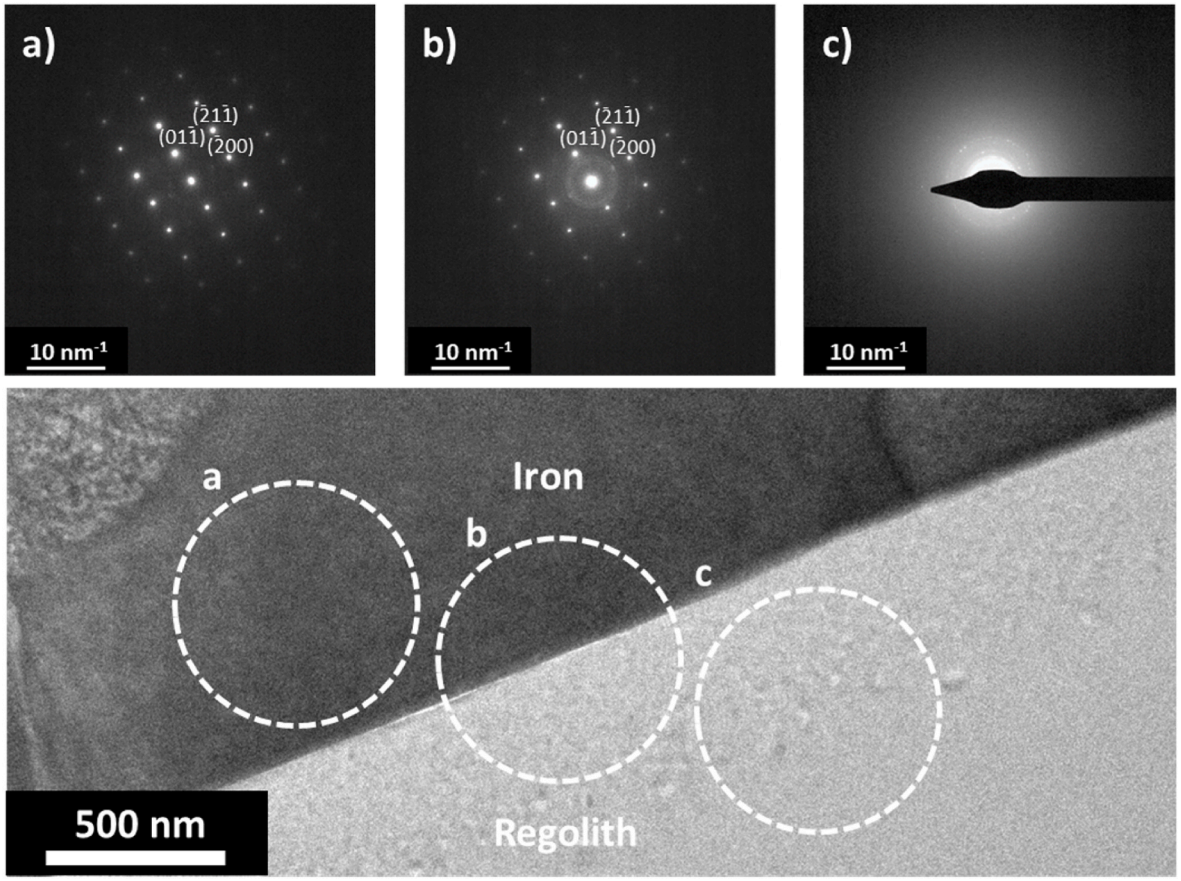

Fig. 8. TEM SAEDP obtained from three distinct regions: the iron matrix (a), Fe-regolith interface (b), and regolith simulant particle (c).

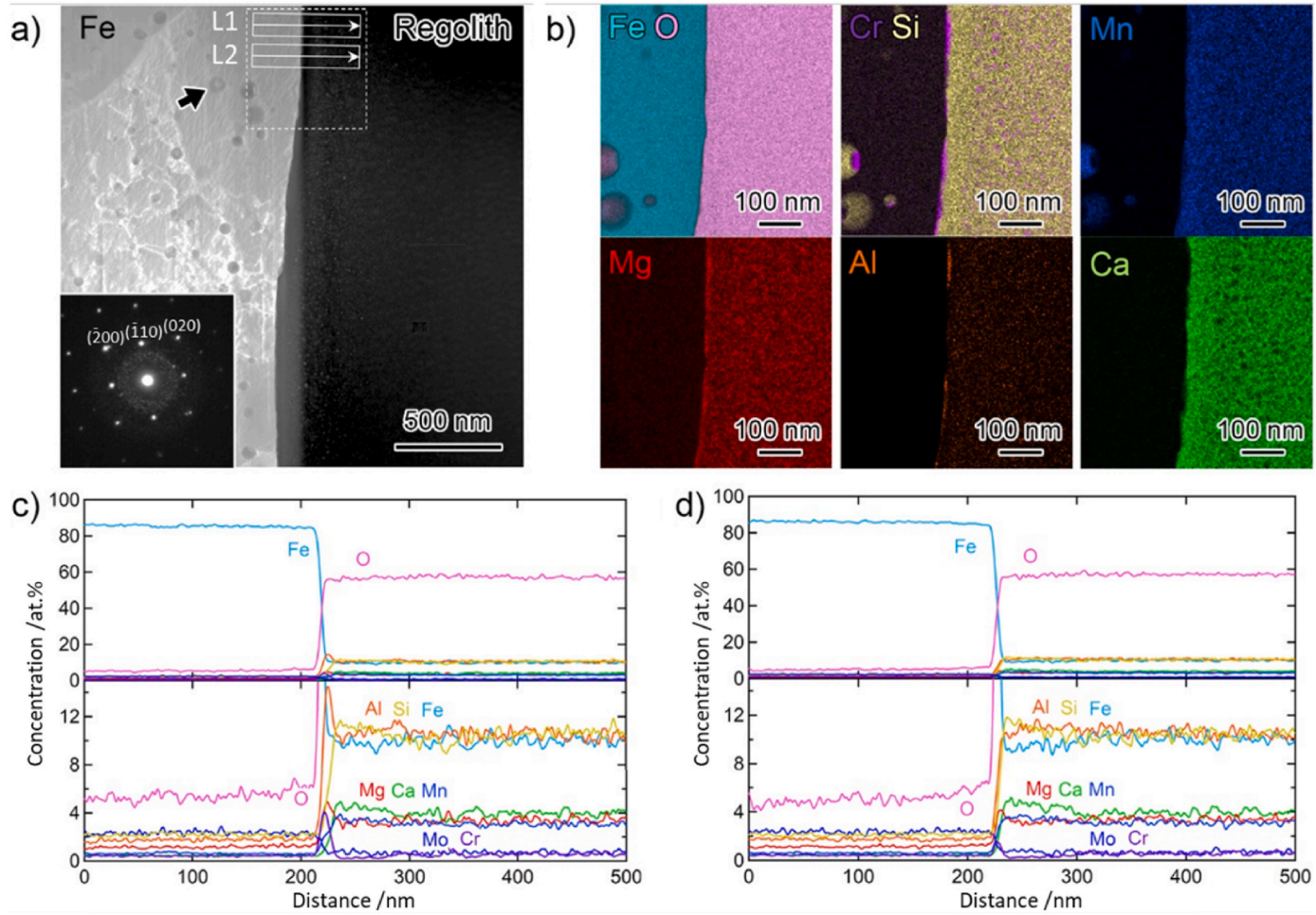

Fig. 9. (a) HAADF-STEM image showing the iron/regolith interface. Inset image is a microbeam electron diffraction (MBED) pattern obtained from a particle in iron phase indicated by an arrow. EDS elemental maps of Fe, O, Cr, Si, Mn, Mg, Al, and Ca obtained from the area indicated by dashed line in (a). EDS line compositional profiles analyzed across the iron/regolith interfaces labeled as (c) L1 and (d) L2 in (a).

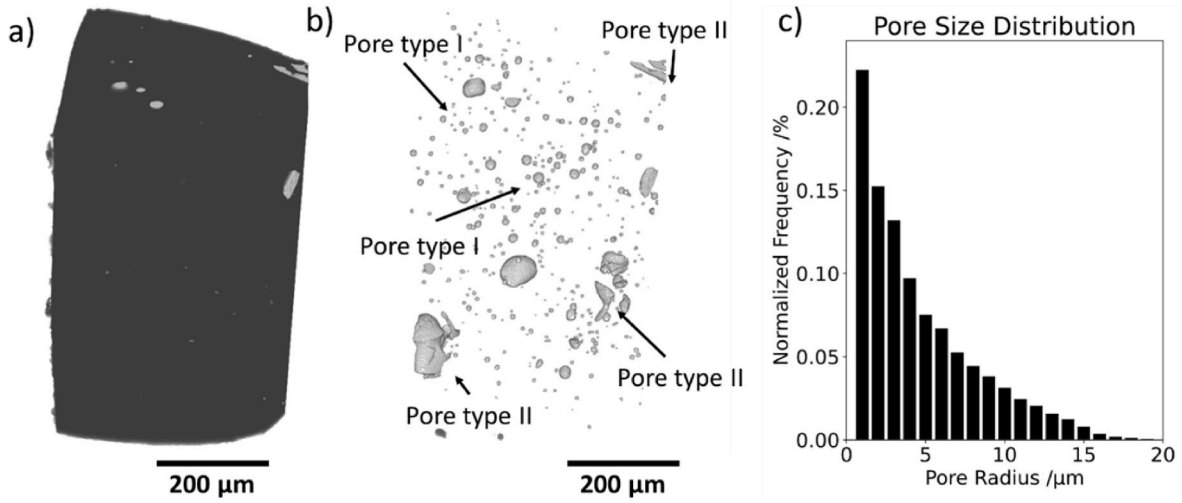

Fig. 10. µ-CT visualizations of a sample volume, showing the sample volume itself and depicting the distribution of pores within the sample (b) and pore size distribution graph (c). Pore type I – spherical pores associated with gas entrapment during L-PBF, pores type II – uneven pores associated with lack of fusion.

net-shaped structure. This leads to the emergence of defects such as cracks and pores. Regolith simulant consists of many different minerals. Interaction between iron melt and these oxides can give us insights into the processes occurring in the interface. The study of Fe-SiO_2 composites remains relatively scarce, with more extensive research focused on the production of Fe-Al_2O_3 metal matrix composites (MMCs). Sintering has been a common method for producing such composite materials. During extended production times, the formation of spinel-type $FeAl_2O_4$ is

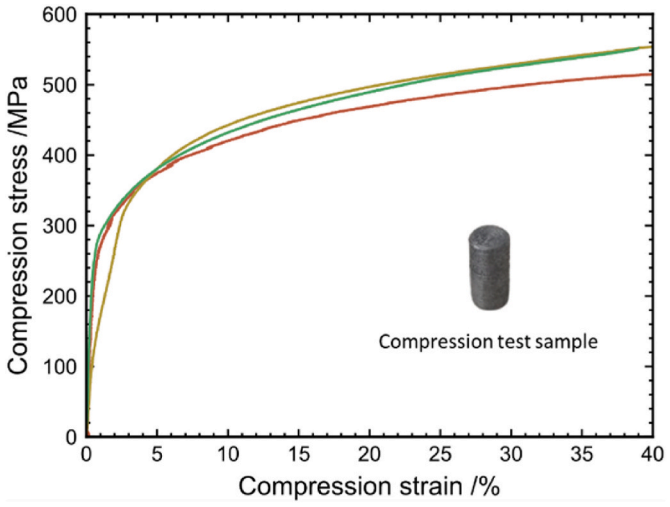

Fig. 11. Mechanical stress-strain curves of the additively manufactured Fe-regolith composite under compression, with three curves representing statistical measures.

typically observed at temperatures around 1170–1370 K [43,44]. This has yet to occur during the L-PBF process of Fe-regolith composites. Moreover, particles remained intact, unlike the behavior previously mentioned [26]. The presence of silicon in iron metallurgy is generally beneficial for steel properties, as it allows the formation of silica in the metal, however, the brittle oxide formed in the process can potentially decrease its mechanical properties. The addition of calcium oxide in steel metallurgy is a known practice to control chemical composition and remove impurities such as phosphorus and fluorene into the slag [45]. Liao et al. [21] have shown that aluminum can reduce silica and form oxides during extended periods in a molten iron pool. Notably, the particle size used in the L-PBF process remained below 50 μm, a crucial consideration to prevent breakage during the thermal shock of the additive manufacturing process [46]. Additionally, Li et al. [47] demonstrated that a regular shape of particles can be more favorable due to the concentration of strains being linked to irregularities in shape. In the context of micro-cracks, irregularly shaped particles tend to generate higher stress concentrations compared to spherical particles, making them prone to brittle fractures, such as irregular WC particles within composites, which can lead to a more brittle Fe_3W_3C phase in the interfacial reaction zones. Consequently, composites with irregular WC particles and an iron matrix exhibited lower yield strength and hardness [47]. Since the regolith simulant particles undergo melting and form a spherical shape, this should positively impact on the mechanical properties of the composite material, yet an increase in mechanical properties remains unobserved.

Oxide nanoparticles, found in the material after the L-PBF process originated from impurities on the surface of initial iron powder. These particles can be found on the surface of water atomized pure iron powder [48]. SEM EDX analysis of the particles on the surface (Fig. 1 (b)) showed that particles 3 and 5 contain manganese and silicon and 2 and 4 also contain chromium. TEM analysis revealed the size of the nanoparticles varies from 20 to 500 nm. TEM-EDX analysis showed that the chromium-based nanoparticles have a regular shape with particles primarily adopting rectangular shapes. Silicon and manganese-based particles have a more spherical shape, which may be due to lower melting point of the silicon and manganese oxide particles. The shape and size of the particles correlate well with work that also looked at nano inclusions with the same chemical composition and inclusion shape when printing different iron-based powders [49]. The mechanical tests conducted showed that the nanoscale particles observed in this work contribute barely noticeable improvement in the mechanical properties of the material. In particular, this is confirmed by the results of the microhardness test, which showed minimal changes in the hardness of the material. Particles overview and TEM EDX mapping are shown in Fig. 12.

Following the L-PBF process, the material exhibits a texturing typical for body-centered cubic (BCC) iron processed with L-PBF, as confirmed by earlier studies [50–52]. The EBSD analysis showed that there is some orientational texturing associated with L-PBF, which corresponds to other investigations [41]; the sizes of the grains are like given in previous studies [42,51,52]. The Rietveld analysis of the metal shown in Fig. 7 further revealed presence of texture. This texture introduces an asymmetry in the shape of the reflections, resulting in a mismatch between calculated and observed diffraction patterns that arise from printing process and not with introduction of particles, this well aligned with previous reports [51,52]. The included 1 wt% regolith simulant intrinsically changes the amorphous scattering content, suggested by its DC of 73 (5) wt.%. The good Rietveld refinement metrics with R_{wp} close to 10 indicate a reliable refinement and an accurate description of the material. Within the nanocrystalline part, all observed Bragg reflections are associated with elemental iron, isotypic to the body-centered cubic W-type, crystallizing in space group $Im\bar{3}m$ with an a-lattice parameter of 286.926 (5) pm, comparable to the findings by Hull [53]. For this phase, an average crystallite size and microstrain of 54 (1) nm and 0.065 (1) %, respectively, were refined. Performing an EnvACS analysis [36] of the Fourier transformed data of the diffraction pattern, providing the pair distribution function (PDF) an ACS of 54.1 (2) nm obtained, providing information about the crystallite size distribution within the sample, which was found to be very broad, with a broadening parameter of 0.99 ± 0.02. The distribution plot of the Fe-regolith samples shown in Fig. 13.

In the L-PBF process, the appearance of a reaction layer between the particle and matrix is observed in the printing of composites [54]. A thin layer of approximately 20 nm is revealed by TEM analysis surrounding each particle, where precipitate and matrix show small chemical interaction. This can be attributed to better stability of the particles with complex chemical composition, while individual oxides tend to dissolve in the molten iron as previously discussed. The short lifetime of the melt pool (time of melt existence in the L-PBF process is in order of ~100 μs), and the stability of the complex particles may be the reason for the absence of a pronounced reaction layer between the particles and the matrix. Regolith simulant consists of many different elements such as Al, Ca, Si, Mg, and many others in forms of minerals, this composition makes it similar to slag, especially after melting and losing the original mineral structure. Studies analyzing the formation of inclusions in molten metals from slags, suggest the crystallization of spinel-type $MgAl_2O_4$ on the metal/particle interface [55]. The formation of spinel crystals and their segregation on the interface, explain the spike in Al and Mg concentration near the surface.

The X-ray μ-CT tomography analysis indicates that the material exhibits an overall low porosity, but persistent macropores are observed. Two types of pores can be distinguished. Type I – pores are smaller and associated with gas entrapment during printing, while type II pores are associated with a lack of fusion. The lack of fusion macropores can be attributed to a substantial alteration in the printing process. The appearance of these types of porosity is due to the presence of two types of particles with significantly different physical properties in the print. The presence of irregular pore shapes is one of the key problems in producing steel matrix composites using the L-PBF process [56]. Porosity volume in this study is significantly higher than in similar studies with pure iron which is again highlighted significant change in L-PBF process after regolith simulant particle introduction [41]. Analysis of SEM images after mechanical testing shows that the regolith simulant particles tend to crack during mechanical loading is shown in Fig. 14.

Microcracks are observed in the particles and at the interface between regolith simulant and Fe matrix. Upon compression, material degradation occurs by detachment of particles from the matrix at the

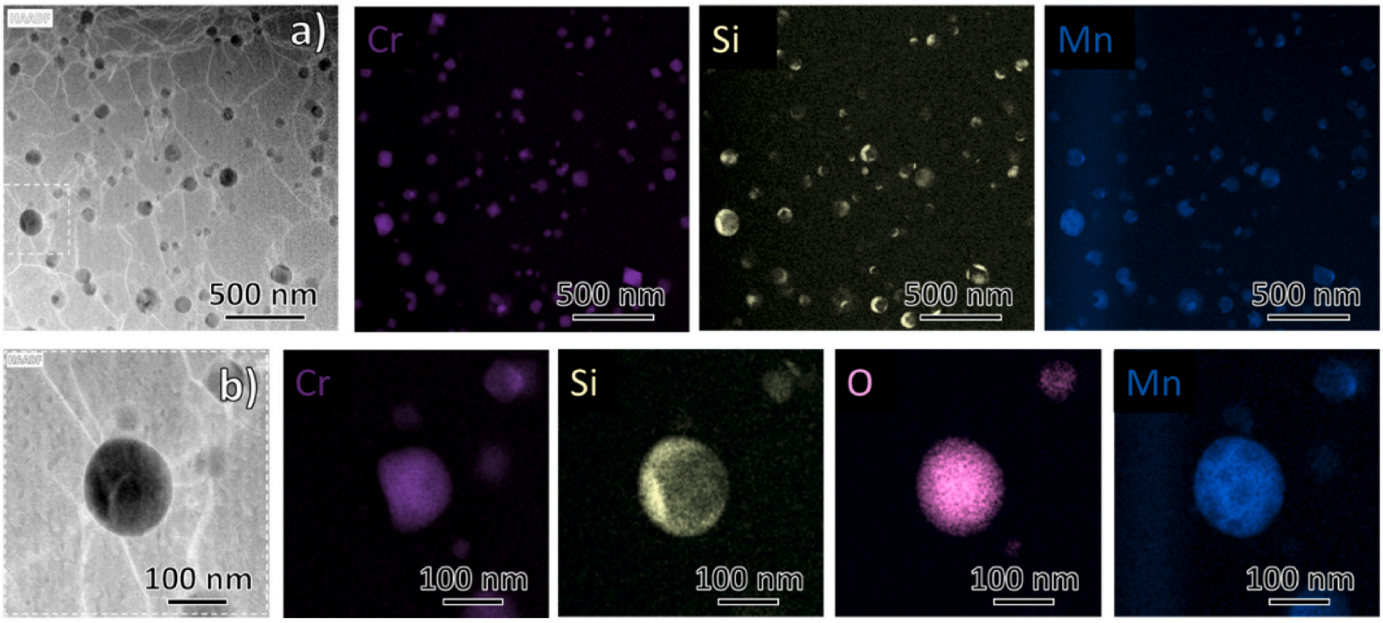

Fig. 12. HAADF images of chromium, silicon and manganese-based nanoparticles and TEM EDX mapping by inclusion elements (a), enlarged images of selected region with several particles and its elemental mapping (b). (For interpretation of the references to colour in this figure legend, the reader is referred to the Web version of this article.)

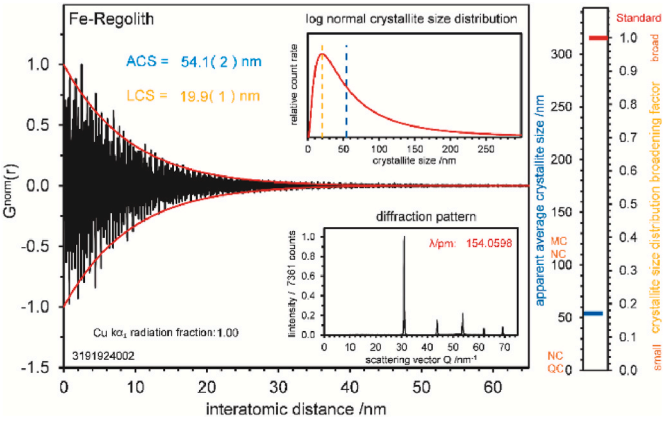

Fig. 13. EnvACS analysis plot for the Fe-regolith sample including the values of the average crystallite size (ACS) and the log normal crystallite size maximum (LCS). In the insets the crystallite size distribution function (top) and the background corrected diffraction pattern (bottom) are given.

interface, which can be seen in Fig. 14. The fracture of the material by this mechanism is most favorable because the interface does not act as a fracture initiation point and also allows stress redirection, which increases the mechanical properties [57]. The material reinforced with brittle particles is highly ductile and withstand a compression of up to 40 %. Breakage of particles and the closure of existing pores are observed, but no cracks propagate from the interface. The mechanical properties of the material, largely associated with suboptimal printing parameters due to the addition of even insignificant amounts of regolith simulant particles, experience a significant decrease. The impact on printability and powder bed formation is noteworthy, emphasizing the importance of maintaining high energy and relatively high scanning speed to prevent particle agglomeration in the melt pool and its reaction with the matrix.

4. Conclusion

The present study successfully demonstrates the feasibility of using laser powder bed fusion (L-PBF) to process iron powder contaminated with regolith, a material representative of extraterrestrial soils such as those found on Mars or the Moon. The Fe-regolith composites with low volume fraction of porosity and a uniform distribution of regolith

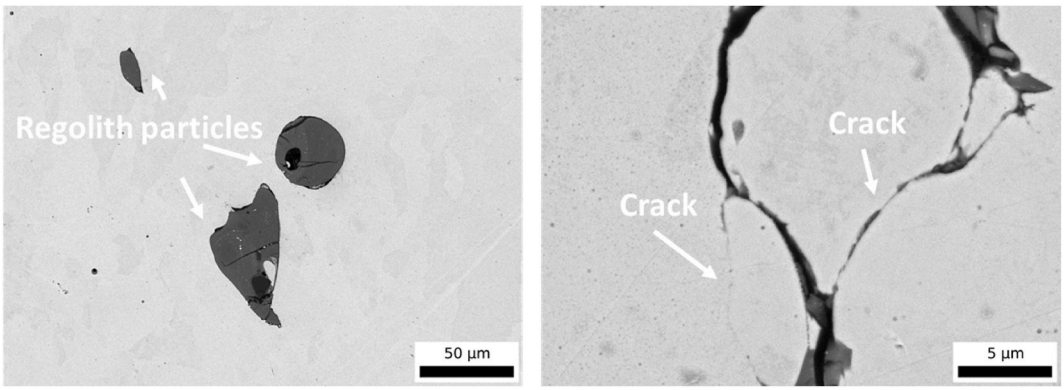

Fig. 14. SEM images of sample after mechanical tests with crack propagation through particles and iron matrix and close up of fractured particles and matrix cracks.

simulant particles within the iron matrix have been obtained and characterized. The original irregular shape of the regolith simulant particles turned spherical after L-PBF, indicating regolith simulant remelting. Scanning transmission electron microscopy analysis revealed the presence of oxide nanoparticles within the iron matrix. These nanoparticles are believed to have formed as a result of contamination during the water-atomization process of the iron powder. The analysis identified these particles as primarily composed of manganese, chromium, and silicon, which are uniformly dispersed throughout the material.

The spherical shape of remelted particles and interface between the iron matrix and the regolith simulant emerged as a key factor influencing the mechanical behavior of the composite material. The interface determines the mechanisms by which cracks initiate and propagate within the material under compression loading. The deformation behavior of the Fe-regolith composite was observed to occur through a mechanism involving the detachment of regolith simulant particles from the iron matrix. Consequently, the spherical shape of the regolith simulant particles within the matrix contributes to the material's integrity by minimizing stress concentrations.

Compression testing of the Fe-regolith composite revealed promising mechanical properties. The composite exhibited a compressive strength of approximately 486.7 $\pm$ 10.6 MPa with over 40 % plastic deformation. Moreover, microhardness tests showed a modest increase in hardness compared to conventionally cast iron, with microhardness value of 169 HV.

This study demonstrates that unavoidable low contamination (below 1 wt%) of materials by Martian regolith simulant upon manufacturing on Mars can be tolerated. This also highlights the potential for utilizing extraterrestrial resources in-situ, e.g. adding regolith to metals to reduce energy costs, to develop sustainable structural materials – an important step toward enabling more complex and autonomous space missions – can be achieved.

CRediT authorship contribution statement

Askar Kvaratskheliya: Writing – original draft, Visualization, Software, Data curation, Conceptualization. **Aleksandr Filimonov:** Writing – review & editing, Validation, Investigation, Data curation. **Bruno Bianchini:** Writing – original draft, Methodology, Investigation, Data curation. **Muchammad Izzuddin Jundullah Hanafi:** Writing – review & editing, Visualization, Methodology, Formal analysis. **Thorsten M. Gesing:** Writing – review & editing, Validation, Methodology, Data curation. **Taisuke T. Sasaki:** Writing – review & editing, Visualization, Investigation, Data curation. **Piter Gargarella:** Writing – review & editing, Validation, Investigation, Data curation. **Lutz Mädler:** Writing – review & editing, Validation, Supervision, Funding acquisition. **Ilya Okulov:** Writing – review & editing, Supervision, Project administration, Conceptualization.

Declaration of competing interest

The authors declare that they have no known competing financial interests or personal relationships that could have appeared to influence the work reported in this paper.

Acknowledgments

The Federal State of Bremen and the University of Bremen support the 'Humans on Mars Initiative' with funding for seven seed projects until the end of 2024. The initiative employs more than 20 early career researchers and supports undergraduate education related to space exploration. https://www.uni-bremen.de/en/humans-on-mars-initiative Authors like to express sincere gratitude to Dr. Tim Grieb (University of Bremen) for his invaluable assistance in the preparation and processing of the Transmission Electron Microscopy data and Dr. Wolf-Achim Kahl (University of Bremen) for his invaluable assistance in the preparation and processing of the μ-computed tomography data.

Data availability

Data will be made available on request.

References

[1] S.O. Starr, A.C. Muscatello, Mars in situ resource utilization: a review, Planet. Space Sci. 182 (2020), https://doi.org/10.1016/j.pss.2019.104824.
[2] NASA, Moon To Mars Objectives, Moon to Mars Objectives: September 2022, 2022.
[3] J.E. Kleinhenz, A. Paz, An ISRU propellant production system to fully fuel a Mars ascent vehicle, in: 10th Symposium on Space Resource Utilization, 2017, 2017, https://doi.org/10.2514/6.2017-0423.
[4] M. Hecht, J. Hoffman, D. Rapp, J. McClean, J. SooHoo, R. Schaefer, A. Aboobaker, J. Mellstrom, J. Hartvigsen, F. Meyen, E. Hinterman, G. Voecks, A. Liu, M. Nasr, J. Lewis, J. Johnson, C. Guernsey, J. Swoboda, C. Eckert, C. Alcalde, M. Poirier, P. Khopkar, S. Elangovan, M. Madsen, P. Smith, C. Graves, G. Sanders, K. Araghi, M. de la Torre Juarez, D. Larsen, J. Agui, A. Burns, K. Lackner, R. Nielsen, T. Pike, B. Tata, K. Wilson, T. Brown, T. Disarro, R. Morris, R. Schaefer, R. Steinkraus, R. Surampudi, T. Werne, A. Ponce, Mars oxygen ISRU experiment (MOXIE), Space Sci. Rev. 217 (2021), https://doi.org/10.1007/s11214-020-00782-8.
[5] B. Ross, S. Haussener, K. Brinkert, Assessment of the technological viability of photoelectrochemical devices for oxygen and fuel production on Moon and Mars, Nat. Commun. 14 (2023), https://doi.org/10.1038/s41467-023-38676-2.
[6] D.L. Linne, G.B. Sanders, S.O. Starr, D.J. Eisenman, N.H. Suzuki, M.S. Anderson, T. F. O'Malley, K.R. Araghi, Overview of NASA technology development for In-Situ resource utilization (ISRU), in: Proceedings of the International Astronautical Congress, IAC, 2017.
[7] B. Khoshnevis, A. Carlson, M. Thangavelu, ISRU-BASED ROBOTIC CONSTRUCTION TECHNOLOGIES for LUNAR and MARTIAN INFRASTRUCTURES NIAC Phase II Final Report, n.d.
[8] R.D. Green, J.E. Kleinhenz, In-situ resource utilization (ISRU) living off the land on the Moon and Mars, in: American Chemical Society National Meeting & Exposition, 2019.
[9] J. Liu, H. Li, L. Sun, Z. Guo, J. Harvey, Q. Tang, H. Lu, M. Jia, In-situ resources for infrastructure construction on Mars: a review, International Journal of Transportation Science and Technology 11 (2022), https://doi.org/10.1016/j.ijtst.2021.02.001.
[10] K.W. Farries, P. Visintin, S.T. Smith, P. van Eyk, Sintered or melted regolith for lunar construction: state-of-the-art review and future research directions, Constr. Build. Mater. 296 (2021), https://doi.org/10.1016/j.conbuildmat.2021.123627.
[11] J. Schleppi, J. Gibbons, A. Groetsch, J. Buckman, A. Cowley, N. Bennett, Manufacture of glass and mirrors from lunar regolith simulant, J. Mater. Sci. 54 (2019), https://doi.org/10.1007/s10853-018-3101-y.
[12] C. Meyers, H. Toutanji, Analysis of lunar-habitat structure using waterless concrete and tension glass fibers, J. Aero. Eng. 20 (2007), https://doi.org/10.1061/(asce)0893-1321(2007)20:4(220).
[13] C. Montes, K. Broussard, M. Gongre, N. Simicevic, J. Mejia, J. Tham, E. Allouche, G. Davis, Evaluation of lunar regolith geopolymer binder as a radioactive shielding material for space exploration applications, Adv. Space Res. 56 (2015), https://doi.org/10.1016/j.asr.2015.05.044.
[14] G.A. Landis, Materials refining for solar array production on the moon. http://www.sti.nasa.gov, 2005.
[15] B.A. Lomax, M. Conti, N. Khan, N.S. Bennett, A.Y. Ganin, M.D. Symes, Proving the viability of an electrochemical process for the simultaneous extraction of oxygen and production of metal alloys from lunar regolith, Planet. Space Sci. 180 (2020), https://doi.org/10.1016/j.pss.2019.104748.
[16] K.D. Grossman, T.S. Sakthivel, L. Sibille, J.G. Mantovani, S. Seal, Regolith-derived ferrosilicon as a potential feedstock material for wire-based additive manufacturing, Adv. Space Res. 63 (2019), https://doi.org/10.1016/j.asr.2018.12.002.
[17] R. Volger, G.M. Pettersson, S.J.J. Brouns, L.J. Rothschild, A. Cowley, B.A.E. Lehner, Mining moon & mars with microbes: biological approaches to extract iron from Lunar and Martian regolith, Planet. Space Sci. 184 (2020), https://doi.org/10.1016/j.pss.2020.104850.
[18] A. Goulas, J.G.P. Binner, R.A. Harris, R.J. Friel, Assessing extraterrestrial regolith material simulants for in-situ resource utilisation based 3D printing, Appl. Mater. Today 6 (2017), https://doi.org/10.1016/j.apmt.2016.11.004.
[19] L. Caprio, A.G. Demir, B. Previtali, B.M. Colosimo, Determining the feasible conditions for processing lunar regolith simulant via laser powder bed fusion, Addit. Manuf. 32 (2020), https://doi.org/10.1016/j.addma.2019.101029.
[20] A. Afrouzian, K.D. Traxel, A. Bandyopadhyay, Martian regolith—Ti6Al4V composites via additive manufacturing, Int. J. Appl. Ceram. Technol. (2022), https://doi.org/10.1111/ijac.14136.
[21] H. Liao, J. Zhu, S. Chang, G. Xue, J. Pang, H. Zhu, Lunar regolith - AlSi10Mg composite fabricated by selective laser melting, Vacuum 187 (2021), https://doi.org/10.1016/j.vacuum.2021.110122.
[22] I.V. Okulov, J. Wilmers, S.H. Joo, S. Bargmann, H.S. Kim, H. Kato, Anomalous compliance of interpenetrating-phase composite of Ti and Mg synthesized by liquid metal dealloying, Scr. Mater. 194 (2021), https://doi.org/10.1016/j.scriptamat.2020.113660.

[23] I.V. Okulov, P.A. Geslin, I.V. Soldatov, H. Ovri, S.H. Joo, H. Kato, Anomalously low modulus of the interpenetrating-phase composite of Fe and Mg obtained by liquid metal dealloying, Scr. Mater. 163 (2019), https://doi.org/10.1016/j.scriptamat.2019.01.017.
[24] A.D. Brandão, R. Gerard, J. Gumpinger, S. Beretta, A. Makaya, L. Pambaguian, T. Ghidini, Challenges in Additive Manufacturing of space parts: powder feedstock cross-contamination and its impact on end products, Materials 10 (2017), https://doi.org/10.3390/ma10050522.
[25] F. Forget, L. Montabone, Atmospheric dust on Mars: a review. 47th International Conference on Environmental Systems, 2017.
[26] New trends in 3D printing. https://doi.org/10.5772/61398, 2016.
[27] H. Chen, D. Gu, K. Kosiba, T. Lu, L. Deng, L. Xi, U. Kühn, Achieving high strength and high ductility in WC-reinforced iron-based composites by laser additive manufacturing, Addit. Manuf. 35 (2020), https://doi.org/10.1016/j.addma.2020.101195.
[28] A. Riquelme, C. Sánchez de Rojas Candela, P. Rodrigo, J. Rams, Influence of process parameters in additive manufacturing of highly reinforced 316L/SiCp composites, J. Mater. Process. Technol. 299 (2022), https://doi.org/10.1016/j.jmatprotec.2021.117325.
[29] A. Perminov, G. Bartzsch, A. Asgarian, K. Chattopadhyay, O. Volkova, Utilization of L-PBF process for manufacturing an in-situ Fe-TiC metal matrix composite, J. Alloys Compd. 922 (2022), https://doi.org/10.1016/j.jallcom.2022.166281.
[30] M.J. Javidi, S.M. Hosseini, F. Khodabakhshi, M. Mohammadi, L. Orovcik, V. Nagy Trembošová, Nagy, M. Nosko, Laser powder bed fusion of 316L stainless steel/Al2O3 nanocomposites: taguchi analysis and material characterization, Opt Laser. Technol. 158 (2023), https://doi.org/10.1016/j.optlastec.2022.108883.
[31] J.F. Qi, C.Y. Liu, Z.W. Chen, Z.Y. Liu, J.S. Tian, J. Feng, I.V. Okulov, J. Eckert, P. Wang, Enhancement in strength and thermal stability of selective laser melted Al–12Si by introducing titanium nanoparticles, Mater. Sci. Eng., A 855 (2022), https://doi.org/10.1016/j.msea.2022.143833.
[32] R. Fayaz, I. Bösing, F. La Mantia, M. Baune, M.I.J. Hanafi, T.M. Gesing, J. Thöming, Deoxidation electrolysis of hematite in alkaline solution: impact of cell configuration and process parameters on reduction efficiency, Chemelectrochem 10 (2023), https://doi.org/10.1002/celc.202300451.
[33] L. Schlüter, A. Cowley, Review of techniques for In-Situ oxygen extraction on the moon, Planet. Space Sci. 181 (2020), https://doi.org/10.1016/j.pss.2019.104753.
[34] K.M. Cannon, D.T. Britt, T.M. Smith, R.F. Fritsche, D. Batcheldor, Mars global simulant MGS-1: a Rocknest-based open standard for basaltic martian regolith simulants, Icarus 317 (2019), https://doi.org/10.1016/j.icarus.2018.08.019.
[35] H.M. Rietveld, A profile refinement method for nuclear and magnetic structures, J. Appl. Crystallogr. 2 (1969), https://doi.org/10.1107/s0021889869006558.
[36] T.M. Gesing, L. Robben, Determination of the average crystallite size and the crystallite size distribution: the envelope function approach EnvACS, J. Appl. Crystallogr. (2024), https://doi.org/10.1107/S1600576724007362.
[37] T.M. Gesing, M.M. Murshed, S. Schuh, O. Thüringer, K. Krämer, T. Neudecker, C. B. Mendive, L. Robben, Nano-crystalline precursor formation, stability, and transformation to mullite-type visible-light photocatalysts, J. Mater. Sci. 57 (2022), https://doi.org/10.1007/s10853-022-07854-w.
[38] C.A. Schneider, W.S. Rasband, K.W. Eliceiri, NIH Image to ImageJ: 25 years of image analysis, Nat. Methods 9 (2012), https://doi.org/10.1038/nmeth.2089.
[39] C.W. Kanolt, The melting-points of some refractory oxides, J. Franklin Inst. 176 (1913), https://doi.org/10.1016/S0016-0032(13)90732-8.
[40] B. Münch, L. Holzer, Contradicting geometrical concepts in pore size analysis attained with electron microscopy and mercury intrusion, J. Am. Ceram. Soc. 91 (2008), https://doi.org/10.1111/j.1551-2916.2008.02736.x.
[41] J. Richter, C.J.J. Torrent, M. Krochmal, T. Wegener, M. Vollmer, T. Niendorf, A comparative study using water atomized and gas atomized powder in laser powder bed fusion – assessment of the fatigue performance, Int. J. Fatig. 168 (2023), https://doi.org/10.1016/j.ijfatigue.2022.107468.
[42] P. Lejček, J. Čapek, M. Roudnická, O. Molnárová, J. Maňák, J. Duchoň, D. Dvorský, M. Koller, H. Seiner, P. Svora, D. Vojtěch, Selective laser melting of iron: multiscale characterization of mechanical properties, Mater. Sci. Eng., A 800 (2021), https://doi.org/10.1016/j.msea.2020.140316.
[43] P. Gupta, D. Kumar, O. Parkash, A.K. Jha, Effect of sintering on wear characteristics of Fe-Al2O3 metal matrix composites, Proc. IME J. J. Eng. Tribol. 228 (2014), https://doi.org/10.1177/1350650113508934.
[44] A. Paesano, C.K. Matsuda, J.B.M. Da Cunha, M.A.Z. Vasconcellos, B. Hallouche, S. L. Silva, Synthesis and characterization of Fe-Al2O3 composites, J. Magn. Magn Mater. 264 (2003), https://doi.org/10.1016/S0304-8853(03)00215-4.
[45] S. Manocha, F. Ponchon, Management of lime in steel, Metals 8 (2018), https://doi.org/10.3390/met8090686.
[46] J. Wang, L. Li, W. Tao, Crack initiation and propagation behavior of WC particles reinforced Fe-based metal matrix composite produced by laser melting deposition, Opt Laser. Technol. 82 (2016), https://doi.org/10.1016/j.optlastec.2016.03.008.
[47] Z. Li, P. Wang, Q. Shan, Y. Jiang, H. Wei, J. Tan, The particle shape of WC governing the fracture mechanism of particle reinforced iron matrix composites, Materials 11 (2018), https://doi.org/10.3390/ma11060984.
[48] J. Wendel, R. Shvab, Y. Cao, E. Hryha, L. Nyborg, Surface analysis of fine water-atomized iron powder and sintered material, Surf. Interface Anal. 50 (2018), https://doi.org/10.1002/sia.6455.
[49] M. Mukherjee, J. Kundu, V.K. Balla, M. Das, K.S. Babu, G.V.M. Krishna, M. Shome, Microstructure and properties of parts manufactured by directed energy deposition of water-atomized low-alloy steel powders, Mater. Sci. Eng., A 814 (2021), https://doi.org/10.1016/j.msea.2021.141232.
[50] H. Zhang, H. Su, Y. Hou, X. Wang, Y. He, F. Li, The microstructure evolution of equiaxed-to-columnar in compositionally graded samples from pure Fe to Fe-27 wt.%Cr fabricated by laser powder bed fusion, Mater. Lett. 330 (2023), https://doi.org/10.1016/j.matlet.2022.133255.
[51] D. Carluccio, M. Bermingham, D. Kent, A.G. Demir, B. Previtali, M.S. Dargusch, Comparative study of pure iron manufactured by selective laser melting, laser metal deposition, and casting processes, Adv. Eng. Mater. 21 (2019), https://doi.org/10.1002/adem.201900049.
[52] M. Zanni, L. Ceschini, A. Fortunato, G. Valli, L. Del Bianco, F. Spizzo, Relationship between microstructure, mechanical and magnetic properties of pure iron produced by laser powder bed fusion (L-PBF) in the as-built and stress relieved conditions, Progress in Additive Manufacturing 7 (2022), https://doi.org/10.1007/s40964-022-00294-7.
[53] A.W. Hull, A new method of X-ray crystal analysis, Phys. Rev. 10 (1917), https://doi.org/10.1103/PhysRev.10.661.
[54] D. Gu, J. Ma, H. Chen, K. Lin, L. Xi, Laser additive manufactured WC reinforced Fe-based composites with gradient reinforcement/matrix interface and enhanced performance, Compos. Struct. 192 (2018), https://doi.org/10.1016/j.compstruct.2018.03.008.
[55] S. Yang, J. Li, L. Zhang, K. Peaslee, Z. Wang, Evolution of Mgo·Al2O3 based inclusions in alloy steel during the refining process, Metall. Min. Ind. 2 (2010).
[56] H. Chen, D. Gu, H. Zhang, L. Xi, T. Lu, L. Deng, U. Kühn, K. Kosiba, Novel WC-reinforced iron-based composites with excellent mechanical properties synthesized by laser additive manufacturing: underlying role of reinforcement weight fraction, J. Mater. Process. Technol. 289 (2021), https://doi.org/10.1016/j.jmatprotec.2020.116959.
[57] V.A. Romanova, R.R. Balokhonov, S. Schmauder, The influence of the reinforcing particle shape and interface strength on the fracture behavior of a metal matrix composite, Acta Mater. 57 (2009), https://doi.org/10.1016/j.actamat.2008.08.046.